Magnetic Resonance Imaging 59 (2019) 88–96

Contents lists available at ScienceDirect

Magnetic Resonance Imaging

journal homepage: www.elsevier.com/locate/mri

Original contribution

Comparison of compressed sensing reconstruction algorithms for ^{31}P magnetic resonance spectroscopic imaging

Alejandro Santos-Díaz[a,b], Michael D. Noseworthy[a,b,c,*]

[a] School of Biomedical Engineering, McMaster University, Hamilton, Ontario, Canada
[b] Imaging Research Center, St. Joseph's Healthcare, Hamilton, Ontario, Canada
[c] Electrical and Computing Engineering, McMaster University, Hamilton, Ontario, Canada

ARTICLE INFO

Keywords:
31P-MRSI
Compressed sensing
EPSI
Low-rank
Hankel matrix

ABSTRACT

Phosphorus MR spectroscopy and spectroscopic imaging (^{31}P-MRS/MRSI) provide information about energy metabolism, membrane degradation and pH in vivo. In spite of their proven utility, ^{31}P-MRS/MRSI are not often used primarily because of the challenges imposed by the low sensitivity and low concentration of metabolites leading to low signal to noise ratio (SNR), coarse spatial resolution and prolonged acquisition time. More recently there has been considerable interest in compressed sensing as an acceleration method for MR signal acquisition. This approach takes advantage of the intrinsic sparsity of the spectral data. In this work, we present a ^{31}P-MRSI sequence that combines a flyback EPSI trajectory and compressed sensing, and we compared two different reconstruction methods, L1 norm minimization and low rank Hankel matrix completion. Our phantom results showed good preservation of spectral quality for both $\times 2.0$ and $\times 3.0$ acceleration factors, using both CS reconstruction methods. However, in vivo ^{31}P-MRS brain data showed the low rank reconstruction approach was most suitable. Overall, this study shows the feasibility of combining a flyback EPSI trajectory and compressed sensing in the acquisition of ^{31}P-MRSI as well as the better suitability of a low rank reconstruction approach.

1. Introduction

Phosphorus MR spectroscopy and spectroscopic imaging (^{31}P-MRS/MRSI) provide information about energy metabolism, membrane degradation and pH in vivo. These methods have been applied in the study of both healthy and disease conditions in different types of tissue such as skeletal muscle and brain [1–5]. In spite of their proven utility, ^{31}P-MRS/MRSI are not often used due to a number of challenges. Specifically, low intrinsic signal to noise ratio (SNR) represents a major limitation as it leads to coarse spatial resolution and very long acquisition times. In addition, relatively short T2 relaxation times of some phosphorus metabolites (i.e. $T2_{ATP} \approx 50$ ms at 3T) make pulse-acquire sequences preferable.

In order to reduce acquisition time while preserving sufficient SNR for spectral analysis, different acceleration methods common in MRI have been translated to ^{31}P-MRSI. Methods such as echo planar spectroscopic imaging (EPSI) [6,7], spiral trajectories [8] and variations of compressed sensing (CS) [9,10] have shown promising results in order to acquire spectra of sufficient quality. More recently, compressed sensing has grown in popularity as an acceleration method for acquisition of MR signals. The basic framework behind it states that it is possible to accurately recover signals from a subset of samples as long as three main criteria are met [11]: (1) The data have a sparse representation in a transformed domain; (2) the aliasing generated due to the sub-sampling scheme is incoherent and (3) a non-linear reconstruction method is to be used in order to enforce consistency with the measurements and sparsity of the data.

The main task in MR spectroscopy is to find a spectrum x from a measured free induction decay (FID) signal y by solving $\mathfrak{F}x = y$, where $\mathfrak{F}$ is the inverse Fourier transform operator. When non-uniform sub-sampling is employed, the problem becomes undetermined and can be expressed as $\mathfrak{F}_u x = \hat{y}$, where $\hat{y}$ is the vector of acquired points filled with zeros at the locations where the signal is not sampled and $\mathfrak{F}_u$ is the undersampled inverse Fourier transform operator. From the different solutions to this problem, the compressed sensing framework seeks to find the sparsest, which is found through L_1 norm minimization as

$$\text{argmin } \|x\|_1 \text{ subject to } \|\mathfrak{I}_u x - \hat{y}\|_2 < \varepsilon \quad (1)$$

* Corresponding author at: McMaster School of Biomedical Engineering, Department of Electrical and Computer Engineering, McMaster University, Engineering Technology Building, ETB-406, 1280 Main St. West, Hamilton, Ontario L8S 4K1, Canada.
E-mail address: nosewor@mcmaster.ca (M.D. Noseworthy).
URL: http://www.ece.mcmaster.ca/~mikenose/web/HOME.html (M.D. Noseworthy).

https://doi.org/10.1016/j.mri.2019.03.006
Received 12 October 2018; Received in revised form 28 February 2019; Accepted 4 March 2019

where ε controls the fidelity of the reconstruction to the measured data.

In the original work of compressed sensing applied to MR images, Lustig et al. proposed a non-linear conjugate gradient algorithm to solve the task [11]. Soon after, the method was extended to applications of hyperpolarized ^{13}C-MRSI experiments as its intrinsic sparsity makes it a natural candidate for CS [12]. Furthermore, the work by Hu et al. established the basis for the development of very fast imaging methods capable of tracking cellular metabolism [13–16].

Development of reconstruction methods for non-uniform sampled signals has also been a focus of research in NMR. A recent comparison [17] points to the strengths and weaknesses of the most common methods used in the field. From this work, the low-rank Hankel matrix completion algorithm [18] is postulated as one of the most robust options to accurately recover the subsampled signals. Briefly, this method exploits the sparsity of a NMR signal from the perspective of finding the solution with the fewest number of spectral peaks rather than finding the spectrum with fewest non-zero values. Thus, the method is less sensitive to fail when reconstructing broad spectral peak signals. It converges on a solution by minimizing the nuclear norm of a Hankel matrix made up of the FID signal.

Under the compressed sensing framework, the purpose of this study was to analyze and compare the performance of two different reconstruction methods, applied to ^{31}P-MRSI data. The first method was the "traditional" compressed sensing (CS) reconstruction first proposed by Lustig et al. [11] and the second, the low rank Hankel matrix completion (LR) recently presented by Qu et al. [18].

1.1. Theory

The CS reconstruction problem based on non-uniform sampling showed in Eq. (1) assumes that the spectrum x is the sparsest solution that matches the measurements ŷ. In the early work of compressed sensing applied to MRI signals [11–13], sparsity was promoted through the use of a Wavelet transformation and a total variation parameter (λ), thus the unconstrained problem in a Lagrangian form can be written as [11]:

$$\min_x \lambda \ ||\psi x||_1 + ||\mathfrak{I}_u x - y||_2^2 \tag{2}$$

where ψ is the Wavelet transform operator and λ is the trade-off between sparsity and data consistency. Here, the L1 norm penalizes many of the small coefficients more than the fewer large coefficients and the parameter λ can be chosen solving the Eq. (2) for different values and choosing λ so that $||\mathfrak{I}_u x - y||_2 \approx \varepsilon$.

The above problem is solved using a nonlinear conjugate gradient descent algorithm with backtracking line search. Details of such algorithm can be found in the Appendix 1 of reference [11].

Another approach to a sparse solution for the problem in Eq. (1) was introduced by Qu et al. [18]. Here, the sparse solution is the one containing the fewest spectral signals rather than non-zero values (as in the above approach). Thus, a spectrum consisting of one, possibly broad, spectral peak is considered strictly sparse. A way to quantify the amount of peaks in a spectrum is to compute the nuclear norm of a Hankel matrix made of the FID signal. A Hankel matrix has the following form:

$$H(y) = Ry = \begin{bmatrix} y_1 & y_2 & y_3 & \cdots & y_Q \\ y_2 & y_3 & y_4 & \cdots & y_{Q+1} \\ \vdots & \vdots & \vdots & \ddots & \vdots \\ y_{n-Q} & y_{n-Q+1} & y_{n-Q+2} & \cdots & y_{n-1} \\ Y_{n-Q+1} & y_{n-Q+2} & y_{n-Q+3} & \cdots & y_n \end{bmatrix} \tag{3}$$

where y_i is the *i-th* measurement point of the fully sampled FID. The nuclear norm of a matrix is the sum of its singular values and it is denoted as $||\ldots||_*$. Thus, the reconstruction problem can be formulated as:

$$\min_y \left(||Ry||_* + \frac{\lambda}{2} \ ||\hat{y} - Uy||_2^2 \right) \tag{4}$$

Here, y is the FID to be estimated, the operator R arranges y into a Hankel matrix, $\hat{y}$ is the vector of measured samples, U is an undersampling operator and λ is a data consistency parameter. The number Q should be chosen so that it is bigger than the number of peaks in the signal. The solution to Eq. (4) is found using an alternating direction minimization method (ADMM). Details of the algorithm are found in the supporting information of reference [18]. It is worth mentioning that this method performs the reconstruction in the time domain, thus the output signal is an FID and the resultant spectrum is calculated as $x = \mathfrak{F}^{-1}y$.

2. Material and methods

2.1. MR system and pulse sequence

All experiments were performed using a 60 cm bore 3 T GE MR750 (GE Healthcare, Milwaukee, WI) scanner (50 mT/m amplitude and 200 T/m/s slew rate gradient system). The pulse sequence developed for this study was built on a recently presented flyback EPSI sequence "*fidepsi*" written in the EPIC programming language (version DV25.R1, GE Healthcare, Milwaukee, WI), due to its flexibility to design the echo planar trajectory [6]. Non-uniform undersampling was achieved by the inclusion of pseudo randomly distributed blips in the G_y dimension during the flyback readout to allow sampling multiple k_f-k_x lines during the same phase encoding step. The pulse duration of the blips was set to be equal to, or slightly less than, the rewinder segment of the EPSI waveform (0.2 84 ms), whereas the amplitude was determined by the pulse sequence to achieve a blip area equal to, or a multiple of, the phase encoding increment. Four different subsampling schemes were implemented in order to achieve acceleration factors ranging from 2× to 4×, using different densities for *k-space* coverage. Fig. 1 shows the pulse sequence diagram and subsampling schemes. The flyback EPSI trajectory was designed to achieve 2.75 × 2.75 cm^2 resolution over an 22 × 22 cm^2 field of view (i.e. 8 × 8 voxels), with a spectral bandwidth of 1428 Hz and 512 spectral points (dwell time = 0 .7 ms, EPSI flat-top duration = 0 .4 ms). Thus, the compressed sensing implementation herein presented further accelerates the already fast EPSI trajectory. Of note, when compared to a fully sampled standard fidCSI, the overall acceleration factors for our "fidepsiCS" approach are ×16, ×24 and ×32. These values are calculated from the number of excitations per average required to sample an 8 × 8 voxels grid, the fully sampled fidCSI requires 64 excitations whereas the fidepsiCS variants require 4, 3 and 2 excitations for the ×16, ×24 and ×32 acceleration factors (Table 1). However, as the fully sampled case is the EPSI trajectory, we refer to the CS acceleration factors as ×2.0 (two fold acceleration, uniform sampling density), ×2.0 w (two fold acceleration, sampling density weighted at the center of *k-space*), ×2.7 (three fold acceleration, sampling density weighted at the center of *k-space*) and ×4.0 (four fold acceleration, uniform sampling density). Further details on the undersampling scheme are mentioned in the caption of Fig. 1.

2.2. Phantom data acquisition

Data collection was performed using an in house designed/built 24 cm diameter quadrature birdcage coil tuned to 51.720 MHz. The pulse sequence was characterized using a custom-built spherical phantom (volume = 1 L, pH = 6.7) containing 25 mmol/L and 10 mmol/L concentrations of sodium phosphate (P1) and phosphocreatine disodium salt (P2) respectively in order to mimic in vivo differences in chemical shift and amplitude. Acquisitions for characterization consisted on collecting six 2D-MRSI datasets using (a) phase encoded MRSI (fidCSI), (b) flyback-EPSI (fidEPSI) and (c) each of the four variation of flyback EPSI combined with compressed sensing

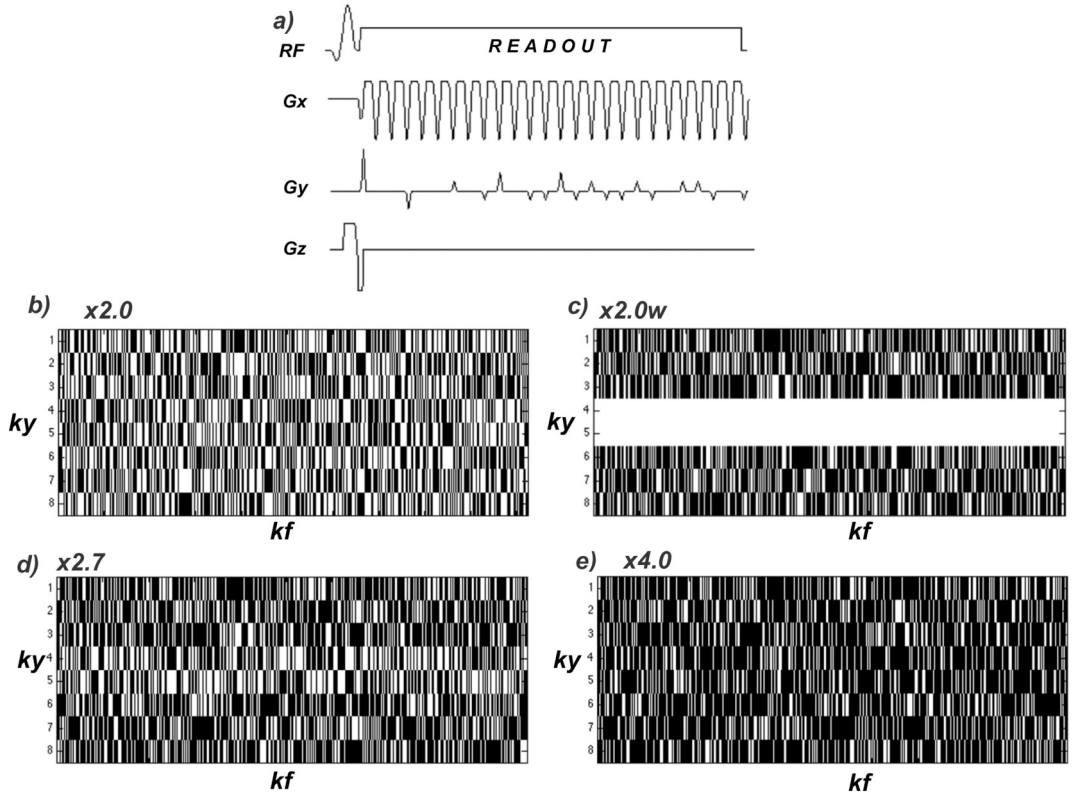

Fig. 1. Pulse sequence diagram (a) and undersampling schedules (b–e). (b) Two fold acceleration with uniform sampling density (×**2.0**), one excitation to acquire every two phase encoding steps. (c) Two fold acceleration with sampling density weighted at the center of *k-space* (×**2.0 w**), first excitation samples first three phase encode steps, second and third fully sample the two central lines and the fourth acquires the later three lines. (d) Three fold acceleration with sampling density weighted at the center of *k-space* (×**2.7**), first excitation acquires the first three lines whereas the second and third sample the two central and three remaining lines respectively. (e) Four fold acceleration with uniform sampling (×**4.0**), first excitation acquires first four lines and the second samples the remaining four. White spaces indicate location of samples, black are absence.

Table 1
Features of each pulse sequence variation. Acq. time: acquisition time. Ex/Avg: number of excitations per average. Acquisition times were calculated by multiplying the number of excitations per average times the number of averages times the repetition time.

Sequence	Averages	Acq. time [min]	Ex/Avg
fidCSI	1	3.2	64
fidEPSI	8	3.2	8
fidepsiCS ×2.0	8	1.6	4
fidepsiCS ×2.0 w	8	1.6	4
fidepsiCS ×2.7	8	1.2	3
fidepsiCS ×4.0	8	0.8	2

(fidepsiCS ×2.0, ×2.0 w, ×2.7 and ×4.0). Radiofrequency excitation was applied using a 1.8 ms asymmetric partially self-refocused sinc pulse, with one side lobe before the main lobe (bandwidth = 2289 Hz). Parameters were matched for all sequences: TR = 3000 ms; flip angle = 50°; FOV = 22 × 22 cm^2; matrix size = 8 × 8; slice thickness = 4 cm; spectral bandwidth = 1420 Hz; spectral points = 512. Four "dummy" scans were used in all acquisitions to allow the system to reach steady state.

2.3. Brain data acquisition

To test the performance of the algorithms using ^{31}P in vivo data, a single fully sampled spectrum was acquired from the parietal lobe of 5 healthy volunteers (24 ± 6 years of age) using a 12.7 cm diameter surface coil (51.705 MHz) matched for brain, a single volume pulse-acquire sequence, squared excitation pulse (0.5 ms, 60° flip angle), 2000 Hz spectral bandwidth, 512 points, 128 averages. The collected FIDs were retrospectively under-sampled (pseudo-randomly selected samples) using 256 (×2.0), 170 (×3.0) and 128 (×4.0) data points to match the acceleration factors of the fidepsiCS sequence, then spectra were reconstructed using 1D implementations of the CS and LR algorithms [17]. The 1D implementation of the CS algorithm corresponds to solving the problem of L1 norm minimization by a soft thresholding conjugate gradient search.

2.4. Data processing and compressed sensing algorithms

All data processing and reconstruction was performed using MATLAB R2015b (The Mathworks, Natick, MA, USA). First, data was re-shaped from the raw blipped acquisition to a raw *fidepsi* format, zero filling the missing sampling points according to the sub-sampling schedule, and then reordered to a 3D matrix of *k-space* data with dimensions k_f-k_x-k_y, used as the input for both reconstruction methods.

The CS reconstruction was performed as follows: (1) data was inverse Fourier transformed in the fully sampled dimension (k_x) to convert the problem to multiple 2D reconstructions, then (2) missing k_y-k_f points were filled using the non-linear conjugate gradient algorithm adapted from the sparseMRI toolbox [11]; (3) the forward Fourier transform was applied in the k_x dimension; and finally (4) data was 3D Fourier transformed. The sparsifying transformation was a 1D length 4 Daubechies Wavelet transform in the spectral dimension, meaning that sparsity of the spectral peaks was presumed and the algorithm tried to minimize the L1 norm of a Wavelet transform of the spectral data. Also, a total variation TV weight was included to promote sparsity of finite differences. The TV and transform weights, as commonly done [11–14], were empirically chosen as 0.015 and 0.005 respectively.

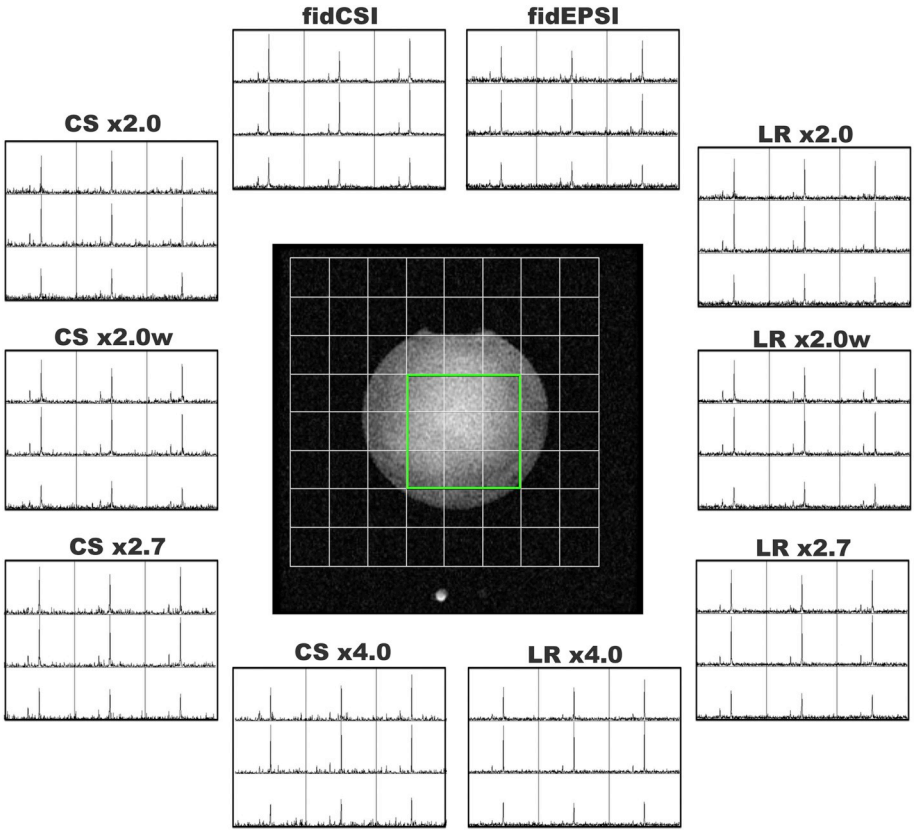

Fig. 2. Example of the acquisition matrix on the reference image and 3×3 voxels region of interest with their corresponding spectra using fidCSI, fully sampled flyback EPSI (fidEPSI) and flyback EPSI combined with compressed sensing (fidepsiCS), using each of the acceleration factors reconstructed with both CS and LR algorithms.

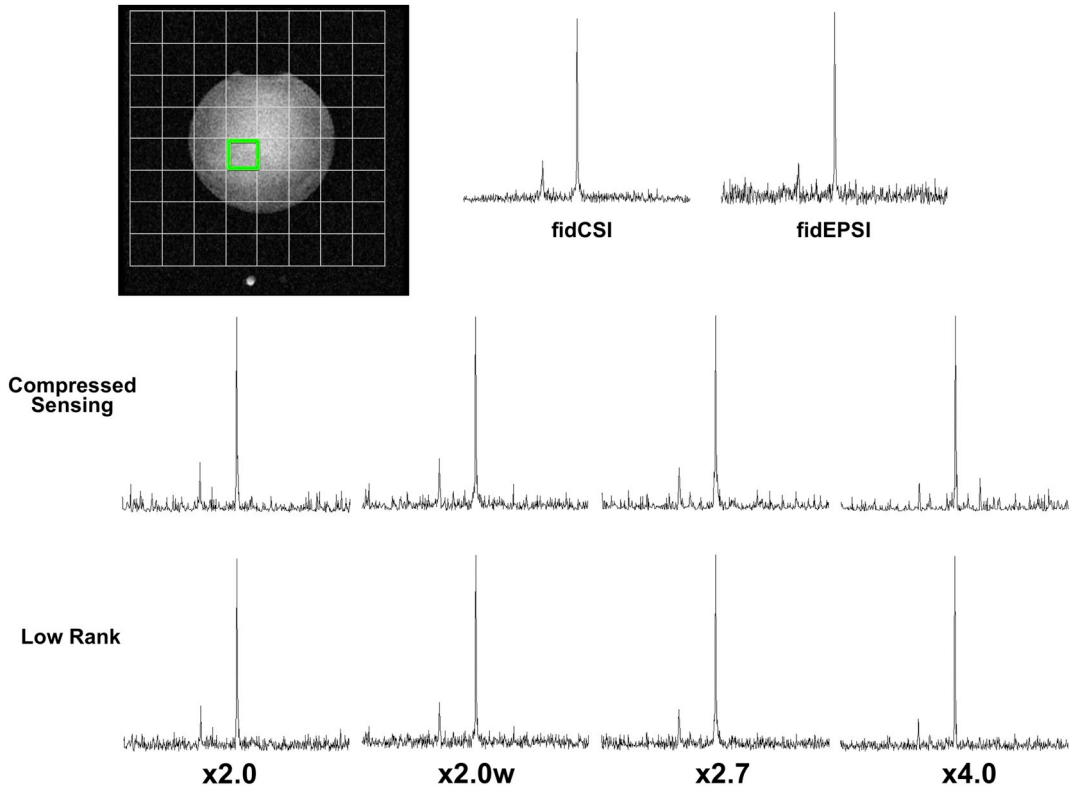

Fig. 3. Sample spectra from the phantom experiments. Each spectrum was taken from the same spatial position (highlighted in green on the spatial reference) to visually compare reconstruction quality. Data is preserved for the $\times 2.0$ and $\times 2.7$ acceleration factors, however the LR algorithm shows fewer artifacts when compared to the CS. (For interpretation of the references to colour in this figure legend, the reader is referred to the web version of this article.)

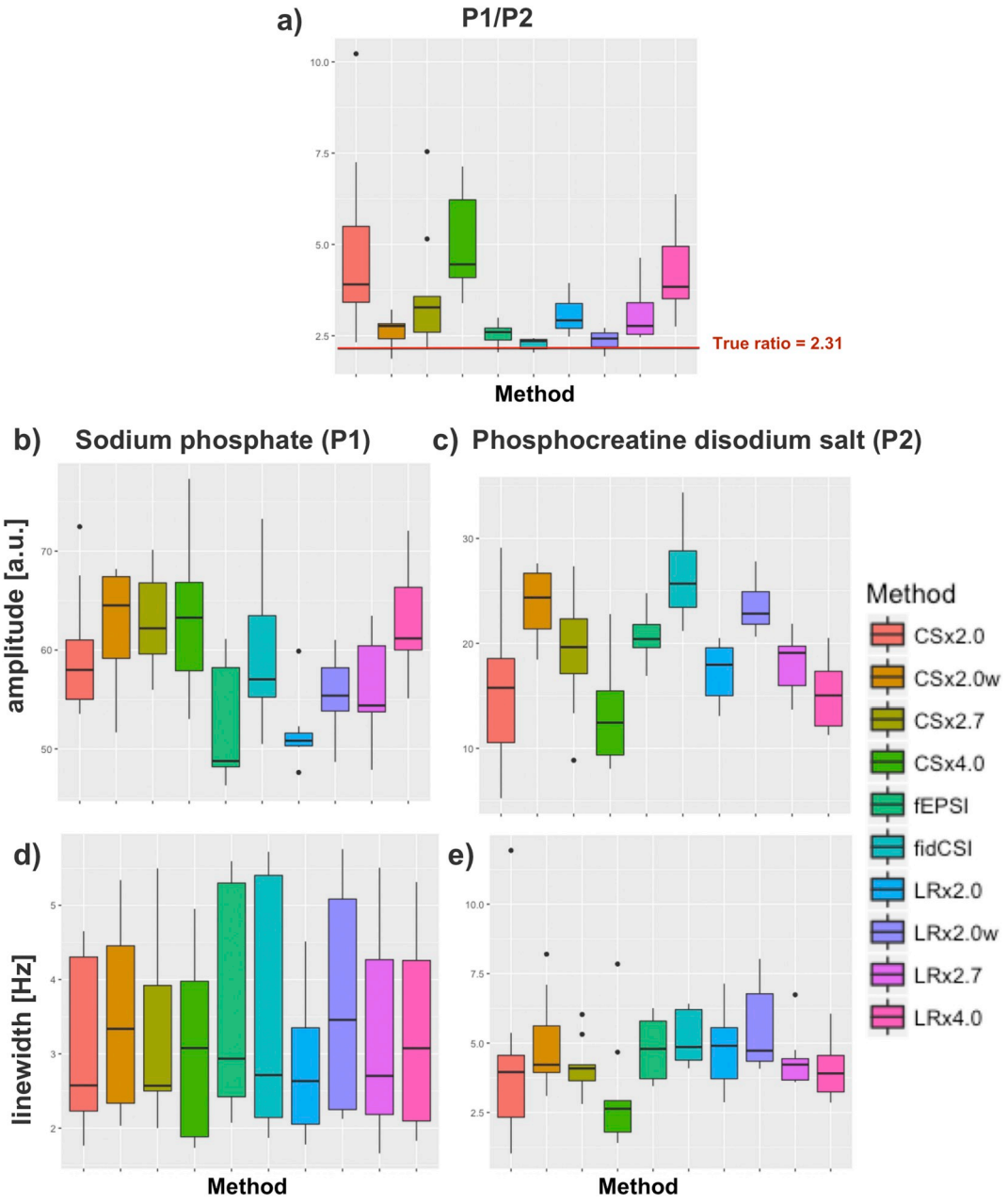

Fig. 4. Box plots for metabolite ratio (a), amplitudes (b,c) and linewidths (d,e) comparing fidCSI, fidEPSI and each of the acceleration factors reconstructed using compressed sensing (CS) and low rank (LR) algorithms. P1: Signal peak from sodium phosphate. P2: Signal peak from phosphocreatine disodium salt. Signal amplitudes are measured in arbitrary units [a.u.]. The truth metabolite ratio in the phantom was 2.31.

Table 2
Metabolite ratios and mean root squared error for the reconstruction of the retrospectively undersampled in vivo data (mean ± SD for 5 volunteers, 24 ± 6 years of age). SNR for the acquisitions was 25.3 ± 8.2. FS: fully sampled fidEPSI. LR: Low rank reconstruction. CS: compressed sensing reconstruction (soft thresholding). Two fold acceleration (×2.0); three fold acceleration (×3.0); four fold acceleration (×4.0). NRMSE: Normalized root mean squared error.

	PCr/PME	PCr/Pi	PCr/PDE	PCr/γATP	PCr/αATP	PCr/βATP	NRMSE %
FS	1.68 ± 0.31	4.94 ± 1.66	0.56 ± 0.10	0.98 ± 0.21	1.29 ± 0.25	1.41 ± 0.28	0 ± 0
LR × 2.0	1.75 ± 0.41	4.37 ± 1.38	0.60 ± 0.13	0.86 ± 0.20	1.32 ± 0.29	1.56 ± 0.39	0.99 ± 0.27
LR × 3.0	1.50 ± 0.21	4.44 ± 2.14	0.52 ± 0.10	0.94 ± 0.23	1.48 ± 0.36	1.49 ± 0.34	1.72 ± 0.39
LR × 4.0	2.31 ± 0.82	2.92 ± 1.90	0.47 ± 0.09	0.67 ± 0.38	1.83 ± 0.40	1.79 ± 0.39	2.73 ± 0.24
CS × 2.0	0.31 ± 0.30	0.41 ± 0.33	0.81 ± 0.82	0.75 ± 0.16	0.70 ± 0.73	0.23 ± 0.18	12.13 ± 0.70
CS × 3.0	0.13 ± 0.1	0.12 ± 0.1	0.33 ± 0.31	0.25 ± 0.18	0.62 ± 0.46	0.06 ± 0.03	12.17 ± 0.69
CS × 4.0	0.94 ± 0.92	1.34 ± 1.46	1.59 ± 1.33	6.14 ± 5.09	0.53 ± 0.37	0.21 ± 0.19	11.9 ± 0.66

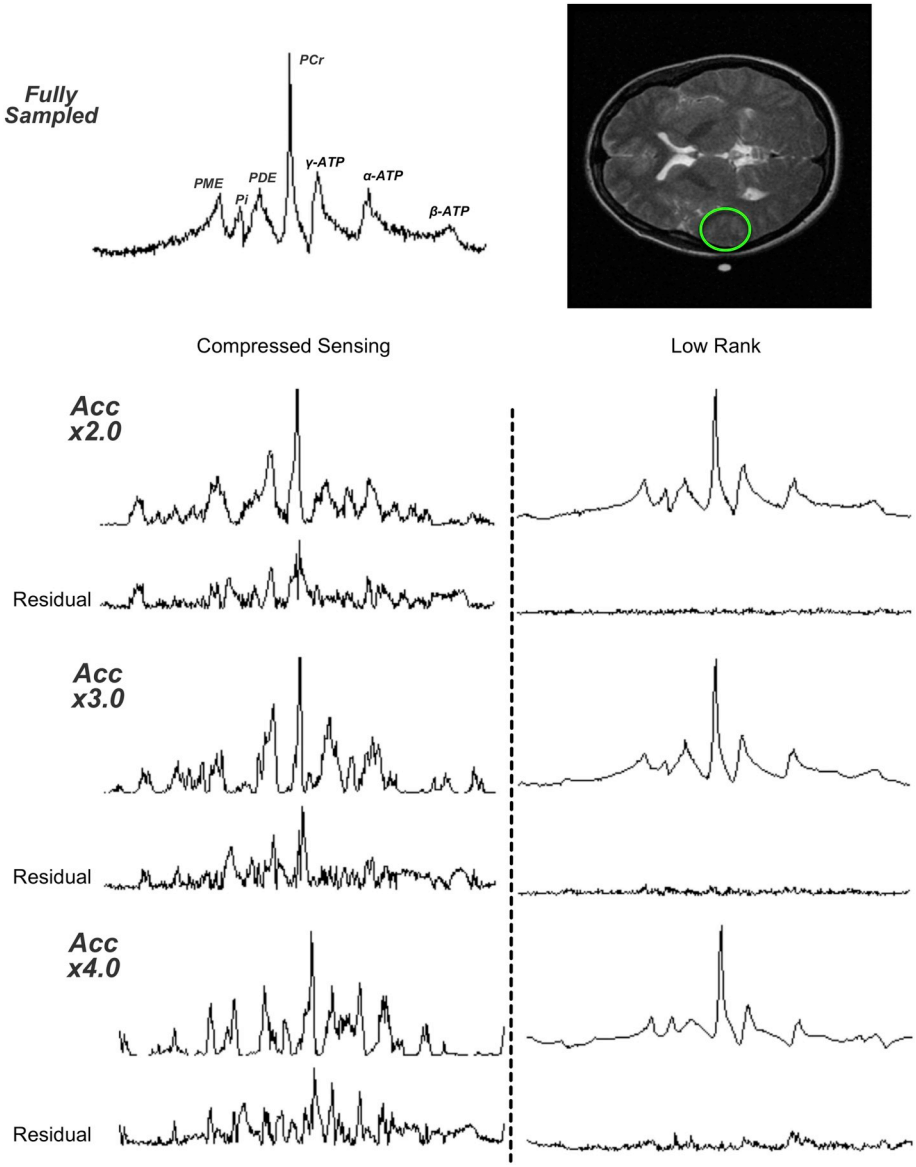

Fig. 5. Comparison of performance between the reconstruction methods. Example of fully sampled brain spectrum with anatomic reference (Top row). CS (left) and LR (right) reconstructions and corresponding residual error for three undersampling schemes. Acc ×**2.0**: using 256 out of 512 points. Acc ×**3.0**: using 170 out of 512 points. Acc ×**4.0**: using 128 out of 512 points. Note that plotted spectra and residual error have the same y-axis scale.

For the LR reconstruction, the 3D matrix of k-space data was (1) reordered as a series of column vectors containing the measured samples from the FID curves of each k_y-k_f plane sequentially; (2) each vector was used to build a Hankel matrix, feeding into an alternating direction minimization method; (3) reconstructed FIDs were reshaped back into a k_x-k_y-k_f array of data that was (4) inverse Fourier transformed in the spatial domain and subsequently Fourier transformed in the spectral dimensions respectively to achieve the 2D MRSI dataset. The data agreement parameter (λ) and reconstruction tolerance threshold (tol) values were empirically determined as 800 and 0.00005 respectively.

To compare performance of the methods, in the phantom experiments we selected a region of interest at the center containing 3 × 3 voxels and measured amplitudes and linewidths from the metabolites. Also, to compare metabolite ratios, we performed statistical analysis using a Kruskal-Wallis test with multiple comparisons. For the in vivo data, we measured metabolite ratios and root mean squared error (RMSE) of the original and reconstructed FID signals. Statistical analysis was also performed to compare metabolite ratios, using ANOVA and Kurskal-Wallis tests. All data fitting was performed using the AMARES implementation in the OXSA toolbox [19]. All statistical analysis was performed using the R software (https://www.r-project.org).

3. Results

Spatial coverage of the data corresponded well between all acquisitions. Fig. 2 shows an example of the 3 × 3 voxel region, near the center of our phantom, and a comparison of spectra acquired using fidCSI, fidEPSI and fidepsiCS with all the acceleration factors for both CS and LR reconstructions. Fig. 3 depicts a single spectrum taken from the same spatial location for each of the sequences tested. The best reconstructions happened for the ×2.0 w variants, as expected due to the fully sampled central *k-space* lines. It is also possible to observe the degradation in spectral quality with higher acceleration factors. To note, the spectra reconstructed with the CS algorithm presents more artifacts when compared to LR.

Results for fitted phantom spectral peak amplitudes and linewidths are shown in Fig. 4. Overall, there was an increase in the P1/P2 ratio for

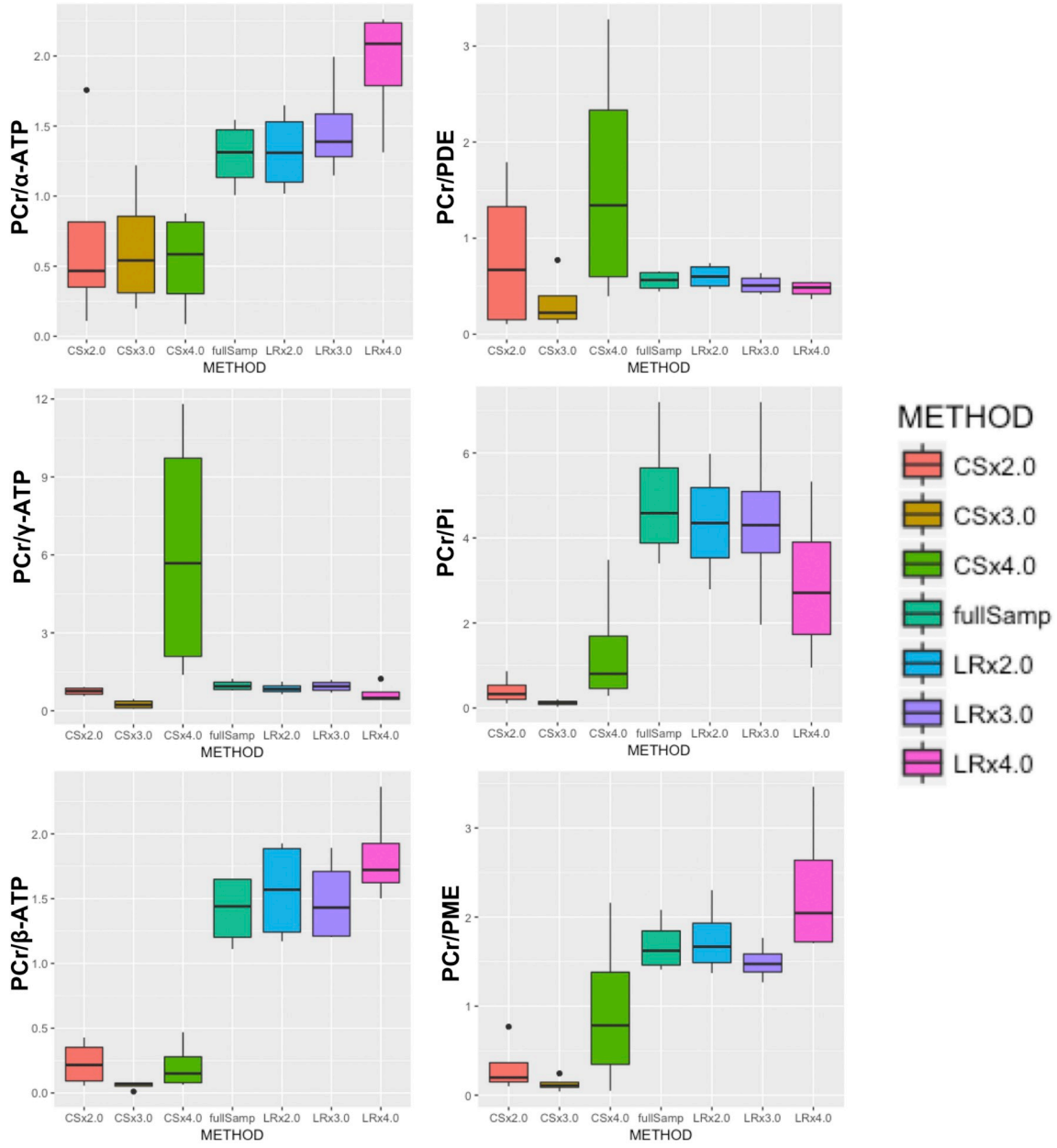

Fig. 6. Box plots for metabolite ratios measured from the brain data after reconstruction using the two methods and all the acceleration factors. CS: compressed sensing. LR: low rank.

higher acceleration factors for both methods, however this overestimation is more accentuated for the CS reconstruction. The statistical analysis showed differences only when comparing the metabolite ratios of fidCSI with CS × 2.0, CS × 4.0 and LR × 4.0, as well as when comparing fidEPSI with CS × 4.0 and LR × 4.0. As expected, best reconstructions occurred for the variants with a higher sampling weight in the center of *k-space* (i.e. ×2.0 w and ×2.7). When analyzing metabolite amplitudes independently, CS reconstructions show a higher overestimation of P1 values compared to LR. On the other hand, for the smaller metabolite (P2), CS reconstructions showed a higher attenuation of the signal, specially depicted in the CS × 2.0 and CS × 4.0. Linewidth values were comparable for all implementations; however, there was a stronger presence of "outliers" for the CS reconstructions.

From in vivo brain acquisition, it is clear that the CS algorithm failed to reconstruct the data. On the other hand, the LR algorithm was capable of achieving reasonable reconstructions, however we observed increasing degradation of spectral quality with higher acceleration factor. Table 2 displays metabolite ratios and root mean squared error (RMSE) for reconstructed spectra. Fig. 5 shows an example of a fully sampled spectrum and the reconstructions for both algorithms with all acceleration factors, as well as the corresponding magnitude error. Based on such residual error, this figure clearly demonstrates two things; first, the CS algorithm is not suitable for reconstruction of ^{31}P-MRS brain data. And second, there is signal degradation with the higher acceleration for the LR method, especially for the smaller metabolite peaks such as Pi, PDE and β-ATP. Additionally, Fig. 6 shows box plots comparing metabolite ratios for the in vivo data. It is evident that the low rank algorithm outperforms the compressed sensing counterpart in the reconstruction of this type of sub-sampled data. The statistical analysis did not show differences when comparing fully sampled with any of the acceleration factors for both methods, however the plots show that results using LR are very similar to the fully sampled version.

4. Discussion

Compressed sensing is becoming a fundamental tool to accelerate acquisition of MR signals. In this work we have compared the performance of two reconstruction algorithms that consider different approaches to the sparse solution, applied to the acquisition of ^{31}P-MRSI data. The first one was the "traditional" compressed sensing reconstruction first proposed by Lustig et al. [11] which seeks the sparse solution as the signal in the frequency domain with the least amount of non-zero values. On the other hand, the low rank Hankel matrix completion approach presented by Qu et al. [18] exploits the sparsity of the NMR signal seeking a solution with the least amount of spectral peaks. From our comparison in the phantom data, the LR algorithm performed better than CS as depicted by the reduced amount of visible artifacts shown in the spectra of Figs. 2 and 3. Additionally, the plots shown in Fig. 4 suggest that although there is signal degradation affecting metabolite ratios for both methods, the CS reconstruction shows the highest deterioration, and the fitted values for LR remain comparable to fully sampled fidEPSI up to the $\times 2.7$ acceleration. Of note, the pulse sequence herein presented further accelerates the acquisition compared to simply the EPSI readout. Thus when comparing to fidCSI, the acceleration factors become $\times 16$, $\times 24$ and $\times 32$ as shown by the number of excitations needed per slice of data (i.e. fidCSI requires 64 excitations for one slice of data whereas the fastest fidepsiCS requires only two).

CS reconstruction was very successful when expanded to hyperpolarized ^{13}C experiments as shown in [12–14]. The main reason for this was the very high SNR of the signal, relatively narrow peak linewidths and reduced number of metabolites. In our work, we extrapolated these methods for the acquisition of ^{31}P MRSI signals where there is an intrinsic low SNR as well as presence of five or more metabolites, all with different amplitudes and linewidths. Thus, based on such differences, especially the broad peaks of some ^{31}P metabolites such as ATP, it was reasonable to suggest that the LR method would perform better, as it approaches the sparsity of the NMR signal seeking for the solution with the least number of spectral peaks, rather than the spectrum with fewer non-zero values. Furthermore, from the same group, Cao et al. presented an improved approach where low rank reconstruction was used [15].

Our results from the phantom experiments suggest a low to moderate superiority of the LR algorithm. To further demonstrate this, results from in vivo brain data showed clear dominance of the low rank approach. Such difference in performance between experiments was due to the fact that the spectrum from the phantom can be considered very sparse as it only contained two metabolites with relatively narrow linewidth, hence the small difference in results. On the other hand, the in vivo spectrum is clearly not sparse in the frequency domain. However, it has a relatively low number of signal components in the time domain, hence it is better suitable for the LR approach. Nonetheless, results showed in Table 2, Figs. 5 and 6 suggest the reconstruction performs well up to a three fold acceleration, consistent with the phantom data as the metabolite ratios were preserved up to the $\times 2.7$ acceleration factor. A limitation for the in vivo experiments is the low sample size, which reduces power of the statistical analysis. However, the plots from Fig. 6 reinforce our results suggesting superiority of the LR approach for this type of data.

When designing the undersampling pattern, from the CS literature we know that the reconstruction will perform better when more samples are acquired at the center of *k-space* [11,14]. Our phantom results are consistent with this, however for the 1D case when retrospective undersampling was used, we found that there was a considerable variation in the reconstruction error and thus quality of spectra was highly dependent on the selected samples (data not shown). The NMR literature has suggested that a noticeable sensitivity enhancement is observed when matching the sampling density with the envelope of the signal [20], however that might compromise the overall quality of the results as there is a tradeoff between the sampling density and incoherence of the aliasing generated. This issue is not within the scope of this study and needs further investigation.

In the present work we targeted the feasibility of this pulse sequence in the acquisition of ^{31}P spectra from the brain and although our results show promise, extremely fast brain acquisitions are rarely needed. On the other hand, ^{31}P-MRS/MRSI has been widely used in the study of muscle dynamics where the high temporal resolution is key [1,2]. Furthermore, our sequence was recently used in the evaluation of PCr/Pi dynamics in skeletal muscle [21]. Another application of accelerated ^{31}P-MRSI would be in the assessment of myocardial metabolites where speed could be an important benefit.

5. Conclusions

We presented a ^{31}P-MRSI pulse sequence that combines a flyback EPSI readout with compressed sensing and compared two different reconstruction algorithms. Our phantom experiments suggested that the LR reconstruction performs better than the CS method. Additionally in vivo brain data acquisition showed the LR reconstruction performed well, when accelerating up to three-fold. Overall, our results suggest that compressed sensing using low rank reconstruction is feasible to accelerate the acquisition of ^{31}P spectroscopic data when relatively low acceleration factors are required.

Acknowledgements

Funding was provided through a CONACYT (Mexico) scholarship granted to ASD (CVU: 304930) and a NSERC Discovery Grant (RGPIN-2017-06318) to MDN.

References

[1] Valkovič L, Chmelík M, Krššák M. In-vivo 31P-MRS of skeletal muscle and liver: a way for non-invasive assessment of their metabolism. Anal Biochem 2017;529:193–215. https://doi.org/10.1016/j.ab.2017.01.018.
[2] Kemp GJ, Ahmad RE, Nicolay K, Prompers JJ. Quantification of skeletal muscle mitochondrial function by 31P magnetic resonance spectroscopy techniques: a quantitative review. Acta Physiol (Oxf) 2015;213:107–44. https://doi.org/10.1111/apha.12307.
[3] Novak J, Wilson M, Macpherson L, Arvanitis TN, Davies NP, Peet AC. Clinical protocols for 31P MRS of the brain and their use in evaluating optic pathway gliomas in children. Eur J Radiol 2014;83:e106–12. https://doi.org/10.1016/j.ejrad.2013.11.009.
[4] Schmitz B, Wang X, Barker PB, Pilatus U, Bronzlik P, Dadak M, et al. Effects of aging on the human brain: a proton and phosphorus MR spectroscopy study at 3T. J Neuroimaging 2018;28:416–21. https://doi.org/10.1111/jon.12514.
[5] Harper DG, Jensen JE, Renshaw PF. Phosphorus spectroscopy (31P MRS) of the brain in psychiatric disorders. EMagRes 2016;5:1257–70. https://doi.org/10.1002/9780470034590.emrstm1463.
[6] Santos-Díaz A, Obruchkov SI, Schulte RF, Noseworthy MD. Phosphorus magnetic resonance spectroscopic imaging using flyback echo planar readout trajectories. Magn Reson Mater Physics, Biol Med 2018;31:553–64. https://doi.org/10.1007/s10334-018-0675-y.
[7] Korzowski A, Bachert P. High-resolution31P echo-planar spectroscopic imaging in vivo at 7T. Magn Reson Med 2018;79:1251–9. https://doi.org/10.1002/mrm.26785.
[8] Valkovic L, Chmelik M, Meyerspeer M, Gagoski B, Rodgers CT, Krssak M, et al. Dynamic 31P MRSI using spiral spectroscopic imaging can map mitochondrial capacity in muscles of the human calf during plantar flexion exercise at 7T. NMR Biomed 2016;29:1825–34. https://doi.org/10.1002/nbm.3662.
[9] Hatay GH, Yildirim M, Ozturk-Isik E. Considerations in applying compressed sensing to in vivo phosphorus MR spectroscopic imaging of human brain at 3T. Med Biol Eng Comput 2017;55:1303–15. https://doi.org/10.1007/s11517-016-1591-9.
[10] Ma C, Clifford B, Liu Y, Gu Y, Lam F, Yu X, et al. High-resolution dynamic 31P-MRSI using a low-rank tensor model. Magn Reson Med 2017;78:419–28. https://doi.org/10.1002/mrm.26762.
[11] Lustig M, Donoho D, Pauly JM. Sparse MRI: the application of compressed sensing for rapid MR imaging. Magn Reson Med 2007;58:1182–95. https://doi.org/10.1002/mrm.21391.
[12] Hu S, Lustig M, Chen AP, Crane J, Kerr A, Kelley DAC, et al. Compressed sensing for resolution enhancement of hyperpolarized ^{13}C flyback 3D-MRSI. J Magn Reson 2008;192:258–64. https://doi.org/10.1016/j.jmr.2008.03.003.
[13] Hu S, Lustig M, Balakrishnan A, Larson PEZ, Bok R, Kurhanewicz J, et al. 3D compressed sensing for highly accelerated hyperpolarized ^{13}C MRSI with in vivo applications to transgenic mouse models of cancer. Magn Reson Med 2010;63:312–21. https://doi.org/10.1002/mrm.22233.

[14] Larson PEZ, Hu S, Lustig M, Kerr AB, Nelson SJ, Kurhanewicz J, et al. Fast dynamic 3D MR spectroscopic imaging with compressed sensing and multiband excitation pulses for hyperpolarized ^{13}C studies. Magn Reson Med 2011;65:610–9. https://doi.org/10.1002/mrm.22650.

[15] Cao P, Shin PJ, Park I, Najac C, Marco-Rius I, Vigneron DB, et al. Accelerated high-bandwidth MR spectroscopic imaging using compressed sensing. Magn Reson Med 2016;76:369–79. https://doi.org/10.1002/mrm.26272.

[16] Chen H-Y, Larson PEZ, Gordon JW, Bok RA, Ferrone M, van Criekinge M, et al. Technique development of 3D dynamic CS-EPSI for hyperpolarized ^{13} C pyruvate MR molecular imaging of human prostate cancer. Magn Reson Med 2018:1–11. https://doi.org/10.1002/mrm.27179.

[17] Shchukina A, Kasprzak P, Dass R, Nowakowski M, Kazimierczuk K. Pitfalls in compressed sensing reconstruction and how to avoid them. J Biomol NMR 2016;68:79–98. https://doi.org/10.1007/s10858-016-0068-3.

[18] Qu X, Mayzel M, Cai JF, Chen Z, Orekhov V. Accelerated NMR spectroscopy with low-rank reconstruction. Angew Chemie - Int Ed 2015;54:852–4. https://doi.org/10.1002/anie.201409291.

[19] Purvis LAB, Clarke WT, Biasiolli L, Valkovič L, Robson MD, Rodgers CT. OXSA: an open-source magnetic resonance spectroscopy analysis toolbox in MATLAB. PLoS One 2017;12:e0185356https://doi.org/10.1371/journal.pone.0185356.

[20] Kazimierczuk K, Orekhov V. Non-uniform sampling: post-Fourier era of NMR data collection and processing. Magn Reson Chem 2015;53:921–6. https://doi.org/10.1002/mrc.4284.

[21] Santos-Díaz A, Harasym D, Noseworthy MD. Dynamic 31 P spectroscopic imaging of skeletal muscles combining flyback echo-planar spectroscopic imaging and compressed sensing. Magn Reson Med 2019;00:1–9. https://doi.org/10.1002/mrm.27682.